Capillary Flow with Evaporation in Open Rectangular Microchannels

Panayiotis Kolliopoulos, Krystopher S. Jochem, Robert K. Lade Jr., Lorraine F. Francis, and Satish Kumar²

Department of Chemical Engineering and Materials Science, University of Minnesota, Minneapolis, MN 55455, USA

Abstract - Numerous applications rely upon capillary flow in microchannels for successful operation including lab-on-a-chip devices, porous media flows, and printed electronics manufacturing. Open microchannels often appear in these applications, and evaporation of the liquid can significantly affect its flow. In this work, we develop a Lucas-Washburn-type one-dimensional model that incorporates the effects of concentration-dependent viscosity and uniform evaporation on capillary flow in channels of rectangular cross section. The model yields predictions of the time-evolution of the liquid front down the length of the microchannel. For the case where evaporation is absent, prior studies have demonstrated better agreement between model predictions and experimental observations in low-viscosity liquids when using a no-slip rather than a no-stress boundary condition at the upper liquid-air interface. However, flow visualization experiments conducted in this work suggest the absence of a rigidified liquid-air interface. The use of the no-stress condition results in overestimation of the time-evolution of the liquid front, which appears to be due to underestimation of the viscous forces from (i) the upper and front meniscus morphology, (ii) dynamic contact angle effects, and (iii) surface roughness, none of which are accounted for in the model. When highviscosity liquids are considered, the large bulk viscosity is found to suppress these factors, resulting in better agreement between model predictions using the no-stress condition and experiments. Model predictions are also compared to prior experiments involving poly(vinyl alcohol) in the presence of evaporation by using the evaporation rate as a fitting parameter. Scaling relationships obtained from the model for the dependence of the final liquid-front position and total flow time on the channel dimensions and rate of uniform evaporation are found to be in good agreement with experimental observations.

¹Present address: Intel Corporation, Portland Technology Development, Hillsboro, OR 97124, USA

²kumar030@umn.edu

Introduction

Capillary flow is the ability of a liquid to flow in narrow spaces without the assistance of, or even in opposition to, external forces. This phenomenon has been vigorously studied since the early 20th century, with much current research focusing on understanding the underlying physical mechanisms as well as exploring a diverse range of applications such as lab-on-a-chip devices, ^{1,2} porous media flows, ³ soil and water repellency, ⁴ heat pipes, ⁵ and printed electronics. ⁶⁻⁸

Microchannels can be classified as closed or open. A closed channel is defined as one where all walls are solid and an open channel as one with a liquid-air interface acting as an effective wall. As a result of advances in lithographic fabrication techniques, open microchannels with various cross-sectional geometries can be fabricated, including, but not limited to, rectangular, 9–12 trapezoidal, 13 U-shaped, 10 and V-shaped. 14 The lack of a top provides access to the inside of the channel. This access can be exploited in applications such as capillary micromolding where cured structures are easily removed from within the microchannels after solidification. 15,16

Capillary flow in closed channels has been extensively investigated experimentally $^{17-21}$ and theoretically. $^{17,19,21-30}$ Theoretical models have focused on describing the liquid-front position x as a function of time t. Lucas 22 and Washburn 23 proposed theoretical models describing flow of a Newtonian liquid in cylindrical capillaries. Both assumed fully developed pressure-driven flow. In Lucas 22 work the driving pressure was the capillary pressure gradient caused by the circular-arc meniscus front. In addition to the capillary pressure gradient, the driving forces considered by Washburn 23 included hydrostatic pressure gradients and an imposed pressure difference between the two ends of the capillary. For a horizontal capillary open at both ends, the hydrostatic and imposed pressure differences are absent, and an analytical solution $x^2 = kt$ is obtained, commonly referred to as the Lucas-Washburn equation, where k is known as the mobility parameter.

Rideal¹⁷ extended the work of Washburn²³ by including inertial effects and assuming that as the liquid enters the capillary, the velocity field is already fully developed. Bosanquet²⁴ also included inertial effects, but instead assumed that the liquid entering the capillary has zero velocity and instantaneously attains a fully developed velocity profile. This assumption allowed Bosanquet²⁴ to obtain an analytical solution describing the time-evolution of the liquid-front position x, which could not be obtained from Rideal's¹⁷ approach.

The initial work of Lucas²² and Washburn²³ has been extended to demonstrate that at early stages the flow is dominated by inertial effects, resulting in $x \sim t$.¹⁹ At later stages the inertial effects are negligible and viscous effects dominate, resulting in $x \sim t^{1/2}$.^{17,22,23} Both scalings have been confirmed experimentally. However, the Lucas-Washburn equation^{22,23} remains the most widely used model for capillary flow in closed microchannels due to its simplicity.

Capillary flow in open microchannels has also been the subject of extensive experimental $^{9-11,14,21,31-34}$ and theoretical $^{10,14,21,35-39}$ investigation, with most studies focusing on V-shaped cross-sectional geometries. $^{14,31-37}$ Experimental investigations of capillary flow in open channels have demonstrated that the scaling of $x \sim t^{1/2}$ seen in closed channels is also observed at later stages. Several researchers 10,21 have modified the Lucas-Washburn equation, 22,23 which was initially developed for closed cylindrical capillaries, to study capillary flow in open channels and have compared model predictions to experimental results. Some studies 10,11 using this modified Lucas-Washburn equation report better agreement with experimental results when a no-slip boundary condition is imposed at the upper liquidair interface, whereas other studies 9,21 report better agreement when a no-stress boundary condition is used. In this paper we address these conflicting results by conducting flow visualization experiments and propose alternative explanations for the discrepancies.

A physical phenomenon present during capillary flow of volatile liquids in open microchannels is evaporation. In certain applications such as microfluidic devices used for diagnostic tests, evaporation can result in undesirable changes in concentration of the test liquid and therefore alter the test results. In other applications such as printed electronics fabrication, the presence of evaporation is exploited by printing electronically active inks on flexible substrates which can be integrated with roll-to-roll manufacturing processes resulting in low-cost and high-throughput device fabrication. Examples of such electronic devices include resistors, capacitors, and transistors.

A drive to minimize the size of printed electronic devices has resulted in a recent effort toward making multilayered electronic devices whose fabrication relies on capillary flow and evaporation within open microchannels. This process is referred to as self-aligned capillarity-assisted lithography for electronics (SCALE).⁶ The SCALE process involves depositing a small volume of conductive ink in reservoirs connected to microchannels. Due to capillary forces, the ink flows down the microchannel. During this filling step, the ink solvent evaporates and conductive particles that were suspended in the ink are deposited on the underlying

substrate to create electronic circuits. Hence, the quality and performance of the printed device relies on controlling the competing phenomena of capillary flow and evaporation.

Experiments on capillary flow in open microchannel networks subject to evaporative lithography were conducted by Lone et al., ¹⁶ where nano- and micro-particle suspensions flowed into and filled the channels. After the flow had reached the end of a channel, subsequent evaporation of the carrier liquid resulted in deposition of the suspended particles on the bottom of the channel, creating a two-dimensional continuous metal pattern. Although particle suspensions were considered, the scaling $x \sim t^{1/2}$ was observed. However, the effect of evaporation during the flow was not investigated.

One of the first studies to investigate the effects of evaporation on capillary flow in open rectangular microchannels was conducted by Lade *et al.*¹² Experiments were conducted in a humidity chamber to control the rate of evaporation. Strong disagreement was observed between the experimental results and the theoretical prediction based on no evaporation (i.e., modified Lucas-Washburn equation^{10,21} subject to a no-slip boundary condition at the upper liquid-air interface), which demonstrates the need for a model that accounts for the effects of evaporation.

In this work, we address conflicting results from prior literature and investigate the effect of uniform evaporation on capillary flow in open rectangular microchannels. We develop a one-dimensional (1D) model that includes effects of concentration-dependent viscosity and uniform evaporation. Capillary flow in the absence of evaporation is initially considered to assess the validity of the no-slip condition that has been used in prior studies. Flow visualization experiments are performed to identify the appropriate boundary condition at the upper liquid-air interface. Potential explanations for the discrepancy observed between experimental observations and model predictions are also discussed. Finally, scaling relationships are obtained from the model and compared to experimental data from Lade et al., 12 showing good agreement.

Problem formulation

Governing equations

We consider an incompressible homogeneous solution of density ρ , viscosity η , and surface tension σ flowing in an open rectangular channel of width W, height H, length L, and inclination angle ψ relative to the x-axis (Figure 1). The solution has a Newtonian solvent

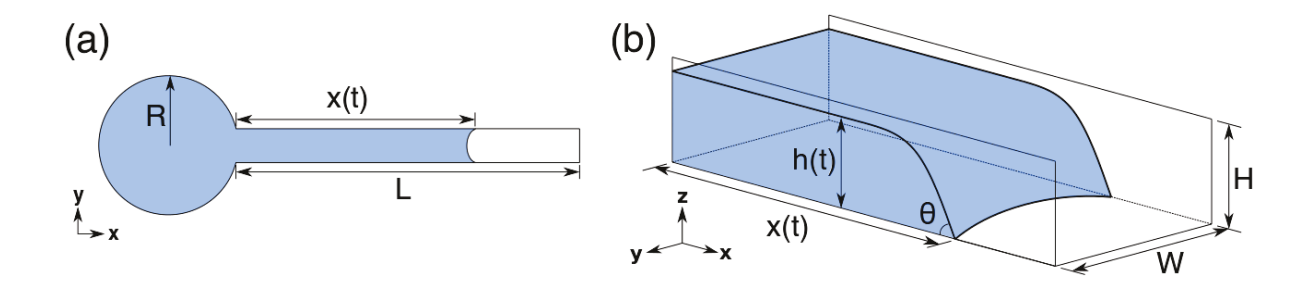


Figure 1: Schematic of liquid undergoing capillary flow in an open rectangular channel. (a) Top view and (b) isoperimetric view.

of density ρ , viscosity η_0 , and surface tension σ_0 . The rectangular channel is connected to a reservoir of radius R. During flow, the solution is subject to a constant uniform evaporative mass flux J. Our theoretical analysis is based on a Washburn²³ and Rideal¹⁷ approach, hence we assume the flow is driven by the capillary pressure gradient caused by the circular-arc meniscus front, while viscous forces resist the flow. Depending on the channel inclination angle, the hydrostatic pressure due to gravity promotes or inhibits liquid imbibition.

We begin with an integral conservation equation for linear momentum in a deformable control volume, $^{26,41-43}$

$$\frac{\partial}{\partial t} \int_{CV} \rho \mathbf{u} dV + \int_{CS} \rho \mathbf{u} [(\mathbf{u} - \mathbf{w}) \cdot \mathbf{n}] dA = \sum \mathbf{F}, \tag{1}$$

where CV and CS refer to the control volume and control surface, respectively, \mathbf{u} is the liquid velocity, \mathbf{w} is the velocity of the control surface, \mathbf{n} is the unit outward normal to the control surface, and t denotes time. Equation (1) equates the rate of change of linear momentum inside the control volume to the momentum flux across the control surface and the sum of the forces acting on the control volume, $\sum \mathbf{F}$.

The control volume is taken to be a rectangular slab of width W, height h(t), and length x(t). We assume a parallel flow, $\mathbf{u}(y,z) = u(y,z)\mathbf{e}_x$, where \mathbf{e}_x is the unit vector in the x-direction. Similar to Rideal, ¹⁷ we assume the liquid already has a fully developed velocity $\mathbf{u}(y,z)$ upon entry into the channel from the reservoir. At the inlet, $\mathbf{w}=0$, and at the liquid front, $\mathbf{w}=\mathbf{u}$. At the upper liquid-air interface, $\mathbf{u}\cdot\mathbf{n}=0$ and $\mathbf{w}\cdot\mathbf{n}=dh/dt$, where h(t) is the liquid height. Note that at the solid walls, $\mathbf{u}\cdot\mathbf{n}=0$ and $\mathbf{w}=0$.

With these assumptions, conservation of linear momentum in the x-direction becomes

$$\frac{\partial}{\partial t} \left[\int_{0}^{x(t)} \int_{0}^{h(t)} \int_{-W/2}^{W/2} \rho u \, dy \, dz \, dx \right] - \int_{0}^{h(t)} \int_{-W/2}^{W/2} \rho u^{2} \, dy \, dz - \int_{0}^{x(t)} \int_{-W/2}^{W/2} \rho u \, \frac{dh}{dt} \, dy \, dx = \sum F_{x},$$
(2)

where $\sum F_x$ represents the x-component of the forces acting on the control volume, and x(t) is the front meniscus position, which, along with the liquid height h, is assumed to depend only on time. General solutions to the Navier-Stokes equation relating u(y,z) to the depthand width-averaged velocity $u_x = dx/dt$ in the form of Fourier series for open^{10,21,45} and closed^{2,27} rectangular channels have been worked out; an example for an open rectangular channel is eq. (32) in the Appendix. The depth- and width-averaged velocity $u_x(t) = dx/dt$ is defined as

$$u_x(t) = \frac{1}{h(t)W} \int_0^{h(t)} \int_{-W/2}^{W/2} u dy dz.$$
 (3)

Upon integration and expansion of the sum of forces acting on the control volume, eq. (2) becomes

$$\rho x h W \frac{d^2 x}{dt^2} + [1 - f_o(\lambda)] \rho h W \left(\frac{dx}{dt}\right)^2 = F_C + F_G + F_V, \tag{4}$$

where F_C are the capillary forces, F_G are the gravitational forces, and F_V are the viscous forces. The expression for the aspect-ratio function $f_o(\lambda)$ resulting from integration of the second term in eq. (2) is given by eq. (34) in the Appendix. If one assumes (as done elsewhere²⁴) that the liquid entering the capillary has zero velocity and instantaneously attains its fully developed velocity profile, then the inlet momentum flux in eq. (2) is zero and the left-hand side of eq. (4) is $(\rho hW)d/dt[x(dx/dt)]$.

Gravitational forces

The gravitational-force term is given by

$$F_G = -\rho g \sin(\psi) hW x, \tag{5}$$

where g is the gravitational acceleration and $\psi = [-\pi/2, \pi/2]$ is the channel inclination angle relative to the x-axis.²¹ If $\psi < 0$ or $\psi > 0$, the gravitational force inhibits or promotes flow, respectively. The limit $\psi = 0$ corresponds to a horizontal channel and the effects of the gravitational force vanish.

Capillary forces

We define the capillary number (ratio of surface-tension to viscous forces) as $Ca = \eta_0 U/\sigma_0$, where U is the characteristic liquid speed. By assuming $Ca \ll 1$, the capillary-force term F_C can be obtained using the approach reported by Good,⁴⁴ which assumes the liquid-front morphology is governed by fluid statics. The total free energy G due to the three-phase contact line moving a distance x in the channel is given by $G = \sigma_{SL}A_{SL} - \sigma_{SV}A_{SV} + \sigma A_{LV}$. Here, σ_{SL} , σ_{SV} , and σ are the surface tensions for the solid-liquid, solid-air, and liquid-air interfaces, and A_{SL} , A_{SV} , and A_{LV} are the areas of those interfaces.

For the geometry we are considering, $A_{SL} = A_{SV} = (W + 2h)x$ and $A_{LV} = Wx\cos(\theta_T)$, where θ_T is the upper liquid-air interface contact angle. We assume the upper liquid-air interface is flat and parallel to the bottom of the channel (i.e., $\theta_T = 0$). For a static contact angle θ satisfying the Young equation, $\sigma\cos(\theta) = \sigma_{SV} - \sigma_{SL}$, the capillary-force term is given by

$$F_C = -\frac{dG}{dx} = \sigma W[\cos(\theta)(1+2\lambda) - 1],\tag{6}$$

where $\lambda = h/W$ is the aspect ratio based on the liquid height. The curvature of the liquidfront meniscus responsible for driving the flow manifests itself via the contact angle θ . Here, θ is the contact angle associated with the front liquid-air interface and the channel walls. This expression for the capillary-force term has been used in prior studies of open microchannels. 9,10,21,45

Viscous forces

The viscous-force term is obtained by assuming a parallel flow, $\mathbf{u}(y,z) = u(y,z)\mathbf{e}_x$, driven by a pressure gradient in the x-direction. As noted earlier, u(y,z) can be related to the depth- and width- averaged velocity $u_x(t) = dx/dt$ via Fourier-series solutions.^{2,27} For closed rectangular channels, these solutions are subject to no-slip boundary conditions at the liquid-solid interfaces. This approach allows for expression of the viscous forces as a function of $u_x(t)$.

Similarly, general solutions are available for open rectangular channels. ^{10,21,45} Conventionally, the boundary condition imposed is no-slip at the liquid-solid interface and no-stress at the upper liquid-air interface. However, Yang et al. ¹⁰ found better agreement with their experiments when considering no-slip at the upper liquid-air interface, which they attributed to contaminant or surfactant accumulation. Therefore, both cases are included in our study.

The final form of the viscous-force term thus depends on the imposed boundary condition at the upper liquid-air interface,

$$F_V = \begin{cases} -\frac{3\eta x}{\lambda \zeta_o(\lambda)} \frac{dx}{dt}, & \text{no-stress boundary condition} \\ -\frac{12\eta x}{\lambda \zeta_c(\lambda)} \frac{dx}{dt}, & \text{no-slip boundary condition,} \end{cases}$$
 (7)

where $\zeta_o(\lambda)$ and $\zeta_c(\lambda)$ are aspect-ratio functions that depend on the boundary condition imposed at the upper liquid-air interface, and are given by eq. (33) and eq. (36), respectively, in the Appendix. A detailed derivation of the expressions for the viscous forces and the aspect-ratio functions can be found in ref. 21.

Conservation of linear momentum

Using the expressions for the gravitational forces (eq. (5)), capillary forces (eq. (6)) and viscous forces (eq. (7)), the expression for conservation of linear momentum (eq. (4)) becomes

$$x\frac{d^2x}{dt^2} + \left[1 - f_o(\lambda)\right] \left(\frac{dx}{dt}\right)^2 = b - g\sin(\psi)x - ax\frac{dx}{dt},\tag{8}$$

where the viscous coefficient a is

$$a = \begin{cases} \frac{3\eta}{\rho W^2 \lambda^2 \zeta_o(\lambda)}, & \text{no-stress boundary condition} \\ \frac{12\eta}{\rho W^2 \lambda^2 \zeta_c(\lambda)}, & \text{no-slip boundary condition} \end{cases}$$
(9)

and the capillary coefficient b is

$$b = \frac{\sigma}{\rho W \lambda} [\cos(\theta)(1+2\lambda) - 1]. \tag{10}$$

Total mass and species balances

The effects of uniform evaporation are considered by assuming the liquid is subject to a constant uniform evaporative mass flux J. The evaporative mass flux is assumed to act only in the region where the liquid height h is spatially uniform (i.e., away from the liquid front). The liquid is assumed to contain a spatially uniform solute concentration $\phi = m_p/(m_s + m_p)$, assuming solvent and solute densities are equal. Here, m_p and m_s are the solute and solvent masses, respectively. Concentration-dependent viscosity $\eta(\phi)$, surface tension $\sigma(\phi)$, and contact angle $\theta(\phi)$ are considered to account for the temporal evolution of the concentration

caused by solvent evaporation. Empirical relations obtained from prior experiments¹¹ are used to describe these concentration-dependent quantities and are presented later in the paper. The effects of evaporation on the shape of the front meniscus are accounted for via the concentration-dependent static contact angle. Note that any direct influence of temperature on surface tension is neglected in this work.

A total mass balance across the upper liquid-air interface⁴⁶ shows that

$$J = \rho \mathbf{n} \cdot (\mathbf{u} - \mathbf{w}) \tag{11}$$

where J is the constant uniform evaporative mass flux through the liquid-air interface, $\mathbf{n} = \mathbf{e}_y$ is the unit normal to the upper liquid-air interface, \mathbf{u} is the liquid velocity field and \mathbf{w} is the velocity of the interface. Since the upper liquid-air interface is assumed to be flat and parallel to the xy-plane, $\mathbf{n} \cdot \mathbf{u} = 0$. Upon rearrangement eq. (11) becomes

$$\frac{dh}{dt} = -\frac{J}{\rho},\tag{12}$$

which is used as the height evolution equation in our model to account for the effects of uniform evaporation.

To account for the time-evolution of the solute concentration ϕ , we make the following species mass balances for the solvent and solute,

$$\frac{dm_s}{dt} = \rho(1 - \phi)hW\frac{dx}{dt} - JWx,\tag{13}$$

$$\frac{dm_p}{dt} = \rho \phi h W \frac{dx}{dt},\tag{14}$$

where the rate of change in mass is equal to the convected mass at the inlet minus the mass lost due to evaporation (only present for solvent).

Scaling

To render the governing equations dimensionless, we scale our variables as follows:

$$x = \mathcal{L}\bar{x},$$
 $t = \mathcal{T}\bar{t},$ $h = W\lambda,$ $m_s = \mathcal{M}\bar{m}_s,$ $m_p = \mathcal{M}\bar{m}_p,$ $J = \frac{\rho\sigma_0}{\eta_0}\bar{J},$ $\eta = \eta_0\bar{\eta},$ $\sigma = \sigma_0\bar{\sigma},$

where the bars denote dimensionless quantities. Here, $\mathcal{T} = \eta_0 W/\sigma_0$ is a characteristic time, $\mathcal{L} = W$ is a characteristic length, and $\mathcal{M} = \rho W^3$ is a characteristic mass. Besides Ca, the other dimensionless parameters that arise are the Reynolds number $Re = \rho UW/\eta_0$ (ratio

of inertial to viscous forces) and the Bond number $Bo = \rho gW^2/\sigma_0$ (ratio of gravitational to surface-tension forces). Note that Re/Ca provides a ratio of characteristic velocities associated with capillarity and momentum diffusion.

Using these scalings, eq. (8) becomes

$$\frac{Re}{Ca} \left[\bar{x} \frac{d^2 \bar{x}}{d\bar{t}^2} + [1 - f_o(\lambda)] \left(\frac{d\bar{x}}{d\bar{t}} \right)^2 \right] = \frac{\bar{\sigma}}{\lambda} [\cos \theta (1 + 2\lambda) - 1] - Bo \sin(\psi) \bar{x} - \bar{\eta} \mathcal{C}(\lambda) \bar{x} \frac{d\bar{x}}{d\bar{t}}, \quad (15)$$

where

$$C(\lambda) = \begin{cases} 3/\lambda^2 \zeta_o(\lambda), & \text{no-stress boundary condition} \\ 12/\lambda^2 \zeta_c(\lambda), & \text{no-slip boundary condition.} \end{cases}$$
 (16)

For horizontal channels (i.e., $\psi = 0$) (or for $Bo\sin(\psi)\bar{x} \ll 1$), the gravitational term can be neglected. For long times (i.e., $\bar{t} \gg Re/Ca$ or $t \gg TRe/Ca$), the inertial term (which $\sim (Re/Ca)\bar{x}^2/\bar{t}^2$) becomes much smaller than the viscous term (which $\sim \bar{x}^2/\bar{t}$). The dimensionless force balance governing the temporal evolution of the dimensionless liquid-front position \bar{x} is then given by

$$\bar{x}\frac{d\bar{x}}{d\bar{t}} = \frac{\bar{\sigma}}{\bar{\eta}\lambda\mathcal{C}(\lambda)}[\cos\theta(1+2\lambda) - 1]. \tag{17}$$

The dimensionless height evolution and species mass balance equations are given by

$$\frac{d\lambda}{d\bar{t}} = -\bar{J},\tag{18}$$

$$\frac{d\bar{m}_s}{d\bar{t}} = (1 - \phi)\lambda \frac{d\bar{x}}{d\bar{t}} - \bar{J}\bar{x},\tag{19}$$

$$\frac{d\bar{m}_p}{d\bar{t}} = \phi \lambda \frac{d\bar{x}}{d\bar{t}}.$$
 (20)

In the absence of evaporation (i.e., $\bar{J} = 0$), eq. (17) has an analytical solution, which in dimensional form is

$$x^2 = kt$$
, where $k = \frac{2\sigma W}{\eta \lambda C(\lambda)} [\cos \theta (1 + 2\lambda) - 1].$ (21)

Here, k is the mobility parameter and has units of $(length)^2/time$. This equation has the same form as the Lucas-Washburn equation^{22,23} but the expression for the mobility parameter is for an open rectangular channel. A similar analysis can be conducted for U-shaped and V-shaped channels to obtain different expressions for k as described in ref. 21. For the remainder of the paper eq. (21) will be referred to as the modified Lucas-Washburn (MLW) equation.

Numerical methods

The system of governing equations (17)–(20) is solved using ode45 in MATLAB, which is a Runge-Kutta method with a variable time step. Initially the channel is considered empty (i.e., $\bar{x}(0) = 0$, $\lambda(0) = H/W$, $\bar{m}_s(0) = \bar{m}_p(0) = 0$). In the absence of evaporation the simulation is terminated after 10^4 dimensionless time units, which exceeds the corresponding dimensionless time of capillary flow typically observed in experiments. When evaporation is present, the simulation is terminated when the liquid-front propagation ceases due to an increase in the viscosity.

Capillary flow in the absence of evaporation

Conflicting results have been observed in previous studies regarding the appropriate boundary condition that should be imposed at the upper liquid-air interface for better agreement with experimental results. Lazouskaya et al.⁴⁷ conducted flow visualization experiments to investigate interfacial interactions and colloid retention under steady flows in an open microchannel. Confocal microscopy was used to track 1.1 μ m diameter fluorescent latex microspheres in an aqueous suspension. While the flow was driven using a syringe pump instead of capillarity, comparison of the experimentally measured and simulated velocity profiles showed better agreement assuming a no-slip boundary condition at the upper liquid-air interface compared to a no-stress boundary condition.

Yang et al.¹⁰ conducted capillary flow experiments in horizontal open rectangular and U-shaped channels using water-glycerol mixtures and observed that the MLW equation (21) shows good agreement with experimental results, provided a no-slip boundary condition at the upper liquid-air interface is considered. Subsequent capillary-flow experiments in open rectangular channels by Sowers et al.⁹ and Ouali et al.²¹ considered horizontal and vertical channels ($\psi = 90^{\circ}$), respectively. Both used high-viscosity polydimethylsiloxane (PDMS) oil and demonstrated agreement with the MLW equation when a no-stress boundary condition at the upper liquid-air interface was considered. Nevertheless, comparison of the experiments and the theory assuming a no-slip boundary condition at the upper liquid-air interface is not explicitly made in these studies.

Recently, Lade¹¹ conducted capillary-flow experiments in horizontal open rectangular channels with water, aqueous glycerol, and a UV-curable resin (NOA73). Lade¹¹ demonstrated that the aqueous mixtures agree best with predictions from the MLW equation when

using a no-slip boundary condition at the upper liquid-air interface, whereas the non-aqueous mixtures agree best when using a no-stress boundary condition. This is in agreement with findings by Yang et al., ¹⁰ Sowers et al., ⁹ and Ouali et al. ²¹ Lade ¹¹ postulated that small surface-tension gradients present naturally in water caused the discrepancy between the aqueous and non-aqueous mixtures, which is the same justification as that proposed by Yang et al. ¹⁰ Such surface-tension gradients cause flows along the liquid-air interface that act to oppose the bulk flow, resulting in an effective immobilization of the liquid-air interface. ⁴⁸

Effect of boundary condition at upper liquid-air interface

To better understand the effect of the boundary condition imposed at the upper liquid-air interface on the model predictions, we consider the case of no evaporation ($\bar{J}=0$). In the absence of evaporation, the model predictions are identical to those of the MLW equation (eq. (21)). The model predictions are compared to capillary-flow experiments by Lade¹¹ and Sowers *et al.*⁹ The physical properties and contact angles of the liquids used in those experiments are shown in Table 1.

Table 1. Dhrzeical	nnon onting and	contact andles	~f	+ 00+	1:
Table 1: Physical	properties and	contact angles	OI	test	nguias

Liquid	Density	Viscosity	Surface tension	Contact angle ^b
	(g/cm^3)	$(mPa \cdot s)$	(mN/m)	(°)
water ¹¹	0.997	0.935	71.4 ± 0.5	19 ± 2^{c}
glycerol (aq.) ^{a,11}	1.167	19 ± 1	67.7 ± 0.7	$25 \pm 2^{\rm c}$
$NOA73 \text{ resin}^{11}$	1.20 ± 0.02	162 ± 3	39.7 ± 0.4	11 ± 2^{c}
PDMS oil ⁹	0.965	4450	19.8	$0_{\mathbf{q}}$

 $^{^{\}rm a}$ Aqueous glycerol with concentration of 0.70 w/w

In the following discussion, the models assuming no-stress and no-slip boundary conditions at the upper liquid-air interface will be referred to as the no-stress and no-slip models, respectively. The comparison of the no-stress and no-slip model predictions to capillary-flow

^bAll channel substrates were plasma treated prior to capillary-flow experiments

^cSolid NOA73 channels

^dSolid PDMS channels

experiments of water, aqueous glycerol, and NOA73 conducted by Lade¹¹ is shown in Figure 2. The no-stress model predictions are represented as a solid line while the no-slip model predictions are represented using a dashed line. The comparison is made for different channel aspect ratios $\lambda = H/W$ (i.e., 46.8/10, 46.8/25, and 46.8/100). For each channel aspect ratio the model predictions are compared to three experimental trials conducted under the same experimental conditions.

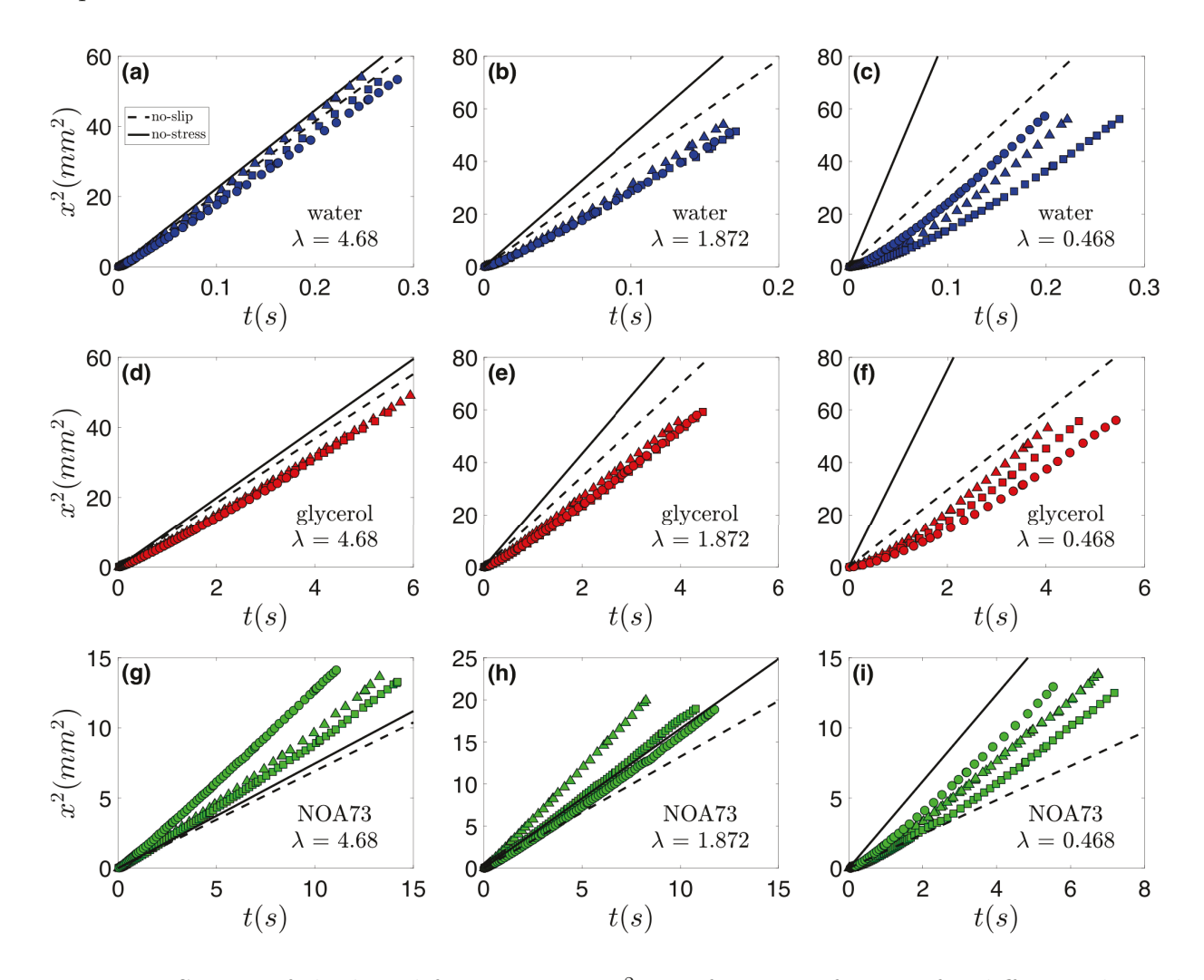


Figure 2: Square of the liquid-front position x^2 as a function of time t for different channel aspect ratios λ with water (a-c), glycerol (d-f), and NOA73 (g-i). The solid and dashed lines represent the model predictions using no-stress and no-slip boundary conditions at the upper liquid-air interface, respectively. The solid symbols represent experimental results for three different trials by Lade, ¹¹ some of which are previously unpublished data.

For all liquids and aspect ratios shown in Figure 2, the liquid-front propagation predicted by the no-slip model is slower compared to that of the no-stress model due to the additional viscous forces that are introduced by imposing the no-slip condition at the upper liquid-air interface. The difference in the model predictions tends to increase as the channel aspect ratio λ decreases. However, it will be shown later that this behavior is non-monotonic.

For solutions of water and glycerol shown in Figures 2a-c and Figures 2d-f, respectively, both the no-slip and no-stress models generally overpredict the liquid-front position compared to experiments. However, the discrepancy is generally less for the no-slip model than for the no-stress model. The opposite is observed for NOA73 which is shown in Figures 2g-h, where the discrepancy is generally less for the no-stress model.

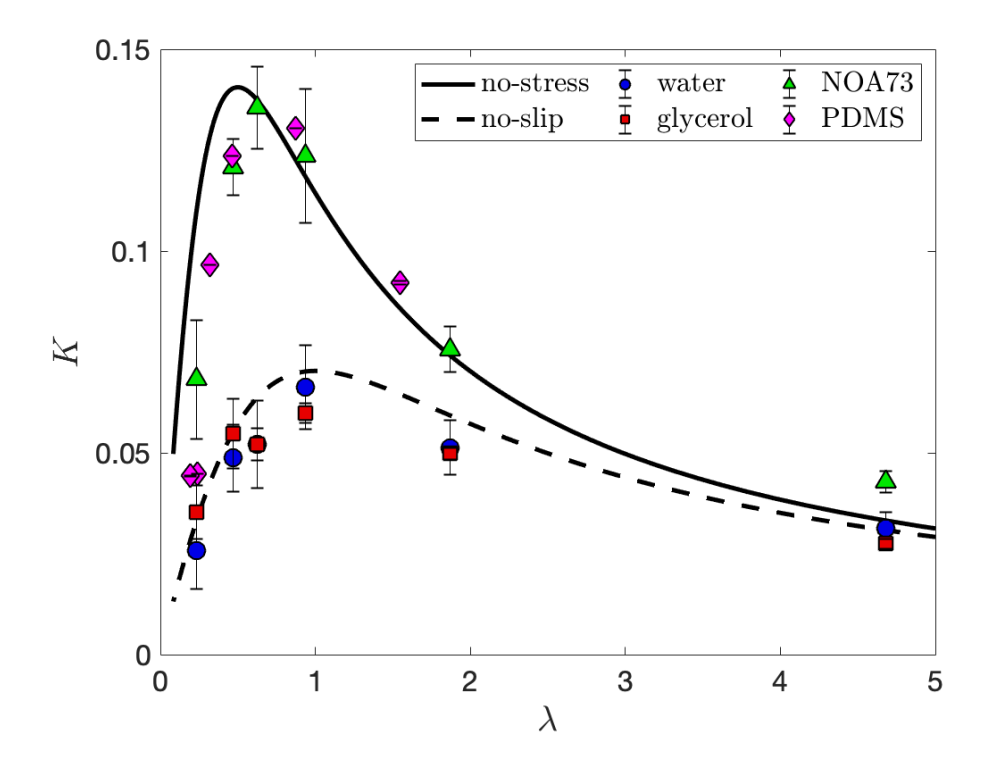


Figure 3: Normalized mobility parameter K as a function of the channel aspect ratio λ for water, ¹¹ glycerol, ¹¹ NOA73, ¹¹ and PDMS. ⁹ The solid and dashed lines represent the model predictions using no-stress and no-slip boundary conditions, respectively. The solid symbols represent experimental results by Lade¹¹ and Sowers et~al. ⁹

To isolate the effect of the boundary condition on the model predictions, we define a dimensionless mobility parameter

$$K = \frac{\mathcal{T}}{\mathcal{L}^2} \frac{k}{\cos(\theta)(1+2\lambda) - 1} = \frac{\mathcal{T}}{\mathcal{L}^2} \frac{2\sigma W}{\eta \lambda \mathcal{C}(\lambda)}.$$
 (22)

The mobility parameter k corresponds to the slope of the model predictions of eq. (21) (Figure 2) and has units of $(length)^2/time$. The non-dimensionalized mobility parameter K

(eq. (22)) is a function of λ and the boundary condition imposed at the upper liquid-air interface. Removing the effects of the liquid-substrate interactions via the contact angle allows for comparison of experimental results for different liquids on different substrates.

In Figure 3, dimensionless mobility parameters obtained from experiments with water, aqueous glycerol, and liquid NOA73 by Lade¹¹ conducted in solid NOA73 channels, and experiments using liquid PDMS by Sowers *et al.*⁹ conducted in solid PDMS channels are compared to model predictions. It is observed that the no-slip model matches the water and aqueous glycerol experiments, while the no-stress model matches the NOA73 and PDMS experiments. Based on Figure 3, the aqueous solutions are in better agreement with the no-slip model predictions, whereas the non-aqueous solutions agree with the no-stress model predictions. These observations are in agreement with those by Yang *et al.*¹⁰ for aqueous solutions, and those by Sowers *et al.*⁹ and Ouali *et al.*²¹ for non-aqueous solutions.

Additionally, a non-monotonic behavior of the difference between the no-slip and no-stress model predictions with increasing channel aspect ratio λ is observed in Figure 3. Specifically, the maximum difference between the two model predictions is observed for $\lambda = 0.761$.

Experiments to test boundary condition

To determine the proper boundary condition at the upper liquid-air interface, we deposited $\sim 25\text{--}35~\mu\mathrm{m}$ diameter Lycopodium particles at the upper liquid-air interface of a 0.70 w/w aqueous glycerol solution flowing in an open rectangular channel and compared the velocity of the particles at the upper interface to the velocity of the liquid front.

Channel fabrication

Traditional microfabrication techniques were applied to form silicon master patterns of capillary channels.⁷ PDMS (Sylgard 184, Dow Corning) was mixed with a base to curing-agent ratio of 10:1 by mass and degassed in a vacuum chamber. The prepared PDMS was then liquid-cast over the silicon wafer in the base of a glass petri dish. The PDMS was cured in an oven at 75°C for 2 hr and then 120°C for 2 hr to fully solidify before being delaminated from the silicon wafer.

Glass slides (75 x 25 mm²) were used as a substrate for the molded capillary channels. A layer of UV-curable optical adhesive (NOA73, Norland Products, Inc.) was placed on top of the glass slides. The PDMS stamp was pressed into the NOA73 and then the assembly was placed in a UV-curing chamber (Honle UV Spot 100, 365 nm) and illuminated at \sim 100 mW/cm² for 90 s to solidify the resin. The PDMS stamp was then peeled off the substrate leaving behind a plastic replica of the capillary channels formed on the silicon master pattern.

Materials preparation and characterization

Aqueous solutions of glycerol with a concentration of 0.70 w/w were prepared using ultrafiltered and UV-treated water (Millipore Synergy filtration system, EMD Millipore). The solution is Newtonian over a wide range of shear rates (1-1000 s⁻¹) and the measured viscosity matched the value reported in Table 1. Lycopodium particles (Duke Scientific) with a diameter range of 25-35 μ m were used as tracer particles for the upper liquid-air interface. Their unique surface structure and hydrophobicity caused by their waxy coating⁴⁹ allowed them to remain at the upper liquid-air interface and prevented sinking into the underlying liquid.⁵⁰

Experimental setup

Prior to the capillary-flow experiments, the microchannels were plasma treated in a plasma cleaner (PDC-32G, Harrick Plasma) at \sim 0.25 Torr and 18 W for 180 s to enhance wetting of the NOA73. The plasma-treated open microchannels were placed under an optical lens (Zoom 6000 system with 3 mm FF zoom lens (model no. 1-6232) and 2x standard adapter (model no. 1-6030, Navitar)). A syringe and needle were used to manually deposit droplets of the aqueous glycerol solution into the center of the reservoir connected to the microchannel. After the solution entered the channel, Lycopodium particles were manually deposited at the upper liquid-air interface at different distances d from the liquid front. Capillary flow of the aqueous glycerol solution was recorded using a high-speed camera (FASTCAM-ultima APX, model 120 K, Photron) at 250 fps and was subsequently analyzed using ImageJ software. The flow was recorded until the liquid-front propagation ceased due to the finite volume of liquid in the reservoir. Experiments were conducted at ambient conditions (23 \pm 1°C, 65 \pm 1% relative humidity). An image sequence of the capillary flow of aqueous glycerol with the hydrophobic Lycopodium particles deposited at the upper liquid-air interface is shown in Figure S1.

From these flow visualization experiments we are able to obtain the velocities of the particles and the liquid front. Comparison of these velocities for three cases is shown in Figure 4 for particles located at three difference distances d from the liquid front. In all three cases, the particle velocity is non zero at the upper liquid-air interface, which suggests the absence of a rigidified liquid-air air interface. Hence, the no-slip boundary condition does not appear to be valid for the system we are considering, which is contrary to what has been reported. Alternative explanations contributing to the discrepancies between the no-stress model predictions and the experimental results are discussed in the next section.

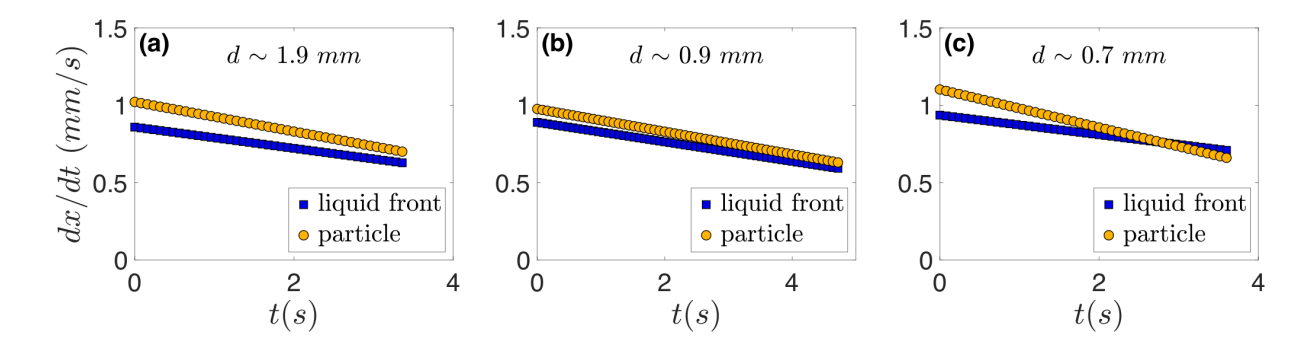


Figure 4: Comparison of the velocity of the $\sim 25\text{-}35~\mu\mathrm{m}$ diameter Lycopodium particles at distances (a) $\sim 1.9~\mathrm{mm}$, (b) $\sim 0.9~\mathrm{mm}$, and (c) $\sim 0.7~\mathrm{mm}$ from the liquid front of the 0.7 w/w aqueous glycerol solution flowing in a 200 $\mu\mathrm{m}$ wide and 177 $\mu\mathrm{m}$ deep open rectangular microchannel.

Potential explanations

Upper meniscus morphology

Sowers et al.⁹ attributed the overprediction of the mobility parameter by the no-stress model to two factors. The first factor is the upper meniscus morphology.⁹ The MLW equation assumes the upper liquid-air interface is flat and the channel to be completely filled. However, experimentally the upper meniscus is observed to have a concave profile^{9,11} and hence the effective height of the liquid is less than the channel height. A lower effective height results in larger viscous forces and therefore a lower mobility parameter.

Forward meniscus morphology

The second factor proposed by Sowers *et al.*⁹ involves the forward meniscus morphology, which the MLW equation assumes is a circular arc. It has been experimentally observed that a curved forward meniscus develops in which the liquid height gradually decreases and finger-like filaments form at the bottom corners of the channels resulting in deviation from a circular-arc meniscus. The finger-like filaments are thought to introduce additional viscous forces leading to a reduction in the mobility parameter.⁹

Seemann et al.⁵¹ elucidated the dependence of the forward meniscus morphology on θ and λ for static liquids. Based on their work, three conditions determine the forward meniscus morphology. The first condition reflects whether capillary imbibition in a rectangular cross-section is energetically favorable, which is true for

$$\cos(\theta) > \begin{cases} \frac{1}{1+2\lambda}, & \text{for } \lambda \ge \frac{\sqrt{2}-1}{2}, \\ \frac{1-4\lambda^2}{1+4\lambda^2}, & \text{for } \lambda < \frac{\sqrt{2}-1}{2}. \end{cases}$$
 (23)

The first expression in eq. (23) is obtained by considering a liquid filament that is in mechanical equilibrium between the force due to the Laplace pressure acting over the whole area of the filament cross section, and the surface tensions acting along the boundaries of this cross section. An alternative method for obtaining this expression is to set dG/dx = 0 in eq. (6) and solve for $\cos(\theta)$ as described in ref. 21. The second expression in eq. (23) is obtained by considering the forces arising from liquid wedges along the groove corners in addition to the Laplace-pressure and surface-tension contributions.

The second condition defining the forward meniscus morphology is the corner-filling condition obtained by Concus and Finn,⁵² which states that for a 90° wedge, imbibition into the wedge will occur for

$$\theta \le 45^{\circ}, \tag{24}$$

which arises from the general stability criterion for capillary surfaces.

The final forward meniscus morphology condition considers whether finger-like filaments are pinned to the top of the side walls of the channel. For $\theta \leq 45^{\circ}$, this is true if

$$\lambda < \frac{1 - \sin(\theta)}{2\cos(\theta)},\tag{25}$$

which is obtained using geometrical arguments by assuming a circular upper meniscus touching the bottom of the rectangular channel while being attached to the top corners of the channel.⁵¹

Equations (23)–(25) were used by Seemann et al.⁵¹ to construct a forward meniscus morphology diagram similar to that seen in Figure 5. Four regions are denoted in the diagram. In region 1 no finger-like filaments are present. In region 2 finger-like filaments are present. However, since they are not pinned to the top corners of the channel they are small in size. In region 3 finger-like filaments are present which are pinned to the top of the channel and are larger in size compared to those observed in region 2. Finally, while capillary flow is observed in regions 1, 2, and 3, in region 4 there is no capillary imbibition.

Experiments by Sowers et al., Lade, and Yang et al. Conducted in horizontal open rectangular microchannels are also depicted in Figure 5. Reported observations from these prior studies for all the experimental data points (shown as solid symbols in Figure 5) agree with the diagram predictions, even though the morphology conditions are defined for static liquid in rectangular channels. The length of the fingers has been seen experimentally and via numerical simulations to increase as λ decreases. Thus, the viscous forces due to the fingers are expected to be larger for longer fingers, which subsequently results in a

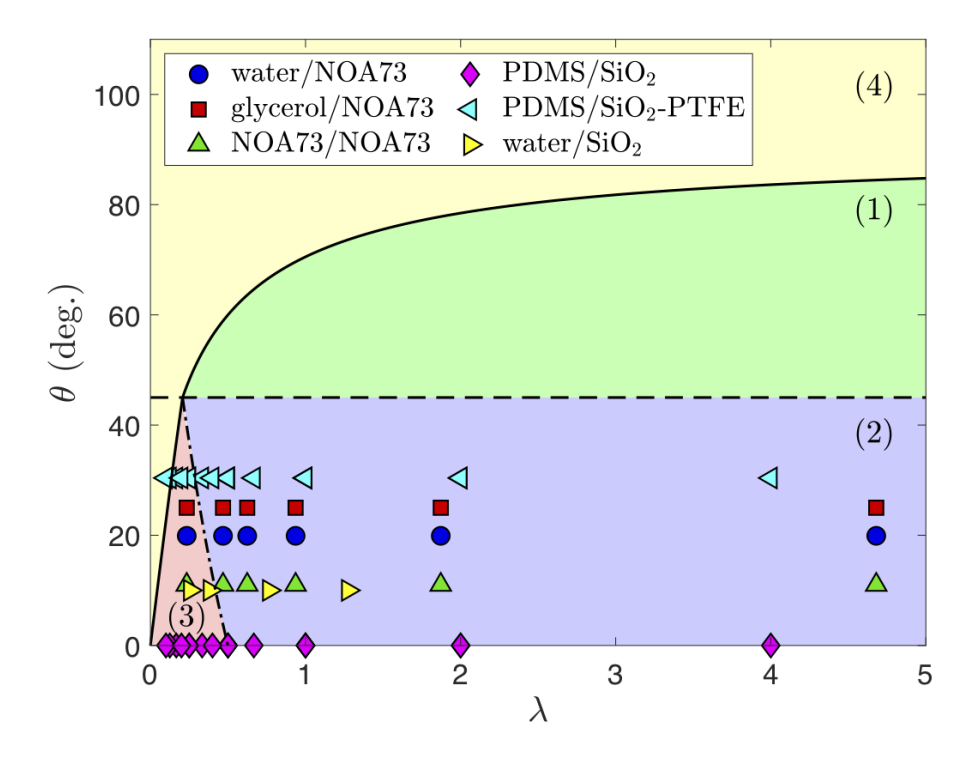


Figure 5: Forward meniscus morphology diagram as a function of static contact angle θ and channel aspect ratio λ . Solid, dashed, and dot-dashed lines are eqs. (23), (24), and (25), respectively. The legend notation indicates the test liquid/substrate material. Solid symbols represent experiments conducted by Lade¹¹ (water/NOA73, glycerol/NOA73, NOA73/NOA73), Sowers *et al.*⁹ (PDMS/SiO₂, PDMS/SiO₂-PTFE) and Yang *et al.*¹⁰ (water/SiO₂) in horizontal open rectangular microchannels. Region 1 has no finger-like filaments present, region 2 has unpinned finger-like filaments, region 3 has pinned finger-like filaments, and region 4 has no capillary imbibition.

larger reduction of the mobility parameter and further deviation from the model predictions, which is consistent with Figure 3.

While numerous experiments in regions 2, 3, and 4 have been conducted, no capillary flow experiments for open rectangular microchannels located in region 1 were found in the literature. In region 1 the MLW equation predictions would be expected to have better agreement with experiments since finger-like filaments are absent in that region and the upper meniscus morphology effects would be reduced compared to those observed in regions 2 and 3 since the static contact angle would be larger. Overall, Figure 5 suggests that to accurately predict the liquid-front evolution in regions 2 and 3, finger formation and dynamics must be accounted for in the model.

Dynamic contact angle

Prior work has suggested that the capillary force used to obtain the MLW equation should be determined by a velocity-dependent dynamic contact angle^{53,54} rather than by the static contact angle to obtain better agreement with experiments. To describe the dependence of the dynamic contact angle θ_d on the liquid velocity $u_x = dx/dt$, we use the hydrodynamic theory of a moving three-phase contact line by $\cos t^{55}$ which assumes the viscosity of the air to be negligible. For $\theta < 3\pi/4$, the Cox theory simplifies to $\theta_d^3 = \theta^3 + 9(\eta u_x/\sigma)\chi$, where χ is the natural logarithm of the ratio between the macroscopic (width of the channel, $\sim 10^{-5}$ m) and the microscopic^{56–58} ($\sim 10^{-9}$ m) length scales.⁵⁵ For the system we are considering the Cox theory has the following form:

$$\theta_d^3 = \theta^3 + 9Ca'\chi$$
, where $Ca' = \frac{\eta}{\sigma} \frac{\mathcal{L}}{\mathcal{T}} \frac{d\bar{x}}{d\bar{t}}$. (26)

Cox's theory⁵⁵ describes the change in the dynamic contact angle due to viscous bending of the liquid-air interface. The theory is derived by applying the method of matched asymptotic expansions to solve the Stokes equations for a moving contact line assuming that Ca' is small and the interface angle is slowly varying. To deal with the stress singularity there, Cox considers a general slip law defined by the ratio of the aforementioned macroscopic to microscopic length scales.

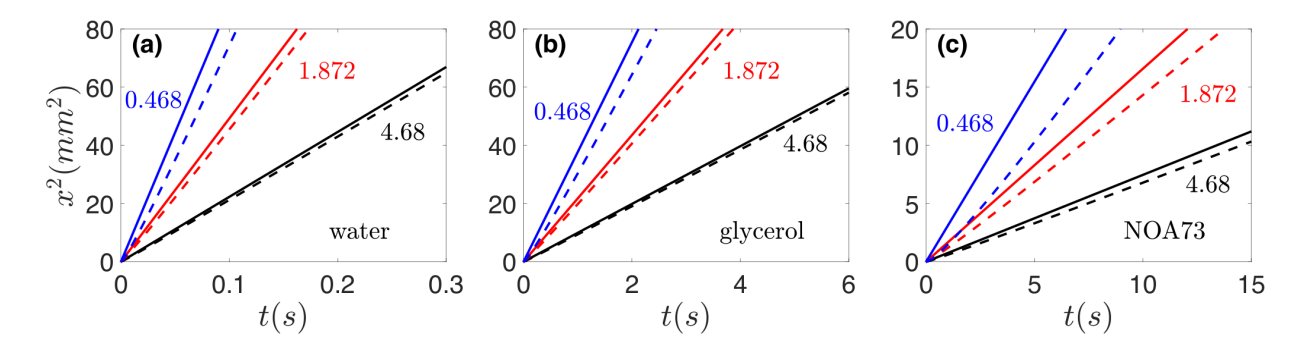


Figure 6: Square of the liquid-front position x^2 as a function of time t for different channel aspect ratios λ of water (a), glycerol (b), and NOA73 (c). The solid lines represent model predictions using a static contact angle. The dashed lines represent model predictions using a velocity-dependent dynamic contact angle⁵⁵ in eq. (26). In all cases $Ca' \sim 10^{-4} - 10^{-2}$.

To evaluate the effect of a velocity-dependent dynamic contact angle, eq. (26) is included to the system of eqs. (17)–(20) and capillary flow in the absence of evaporation (i.e., J=0) is considered. The effect of a velocity-dependent dynamic contact angle on the liquid-front

evolution for water, glycerol, and NOA73 is depicted in Figure 6. It is observed that using the velocity-dependent dynamic contact angle results in a slower predicted liquid-front evolution compared to using a static contact angle. Additionally, for all three liquids decreasing the channel aspect ratio results in larger deviation from the model predictions using the static contact angle. This is expected since for the three aspect ratios we are considering, decreasing λ results in an increase of the flow velocity as observed in Figure 2. However, it is important to note that based on Figure 3 this trend is not monotonic, and therefore a decrease in λ does not always result in an increase of the flow velocity.

For the low-viscosity liquids (i.e., water and glycerol) in Figures 6a,b the effect of the dynamic contact angle is less pronounced than that for the high-viscosity liquid (i.e., NOA73) in Figure 6c. While the velocities for the low-viscosity liquids are larger than those of the high-viscosity liquid, the multiple order-of-magnitude difference in the viscosity results in a larger capillary number Ca' for the high-viscosity liquid and therefore a larger deviation from the model prediction using the static contact angle. These observations are in agreement with those by Popescu $et\ al.$,⁵⁴ who observed a larger deviation from the model predictions using a static contact angle of a high-viscosity silicon oil compared to water for capillary rise in tubes.

It is important to note that dynamic contact angles decrease with geometric confinement, 59,60 which the Cox theory does not account for. Effects of geometric confinement are significant when the channel width W is much smaller than the liquid's capillary length $l_{cap} = \sqrt{\sigma_0/\rho g}$, 61 or equivalently when the Bond number $Bo = \rho g W^2/\sigma_0 \ll 1$. For the microchannels and liquids considered in this study, confinement effects appear to be significant since $Bo \sim 10^{-11} - 10^{-8}$. Additionally, the dynamic contact angle depends on the ratio of the macroscopic and microscopic length scales, and it is not clear what to use for those values. (The values used above are chosen simply to demonstrate qualitative differences in the model predictions using dynamic and static contact angles.) In order to properly account for dynamic contact angle effects, highly resolved finite element method simulations would be necessary.

Surface roughness

An additional potential factor for the discrepancy between the model predictions and the experiments is the roughness of the channel. Girardo $et\ al.^{62}$ conducted experiments and Lattice Boltzmann simulations to study the effect of forward meniscus morphologies in smooth and rough closed microchannels at short time scales. It was illustrated that even nanoscopic channel roughness introduces extra dissipative forces, resulting in slower capillary filling (i.e., lower mobility parameter) and therefore better agreement with experimental observations. Surface roughness can be incorporated in the model by replacing the static contact angle θ in eq. (6) by the Wenzel (if the liquid fully penetrates into the surface features) or the Cassie-Baxter (if liquid bridges are formed between the surface features) contact angles.²¹ However, this approach to incorporate surface roughness is not able to account for contact-line pinning and contact-angle hysteresis.

Bulk viscosity

While the factors discussed above provide potential explanations for the overprediction of the mobility parameter by the no-stress model, they do not provide an explanation for the discrepancy observed between the aqueous and non-aqueous mixtures seen in Figure 3. A potential explanation for this is the difference in the bulk viscosity that is observed between the aqueous and non-aqueous mixtures seen in Table 1. Due to the non-aqueous mixtures having a higher viscosity compared to the aqueous mixtures, any of the aforementioned potential factors that result in lowering of the mobility parameter are suppressed by the large bulk viscosity. Hence, better agreement is observed between the no-stress model predictions and high-viscosity mixtures not due to the non-aqueous nature of these liquids but rather due to their high viscosity.

We note that a combination of the factors discussed above may be responsible for discrepancies between model predictions and experimental results. This uncertainty means that rather than being a truly predictive model, the MLW equation has mostly been used to fit experimental data by using the mobility parameter k as a fitting parameter instead of calculating it analytically.^{11,16,21} Development of a more detailed model is needed to make more quantitative predictions and to determine which factors are most responsible for discrepancies between theory and experiment.

Capillary flow in the presence of evaporation

To elucidate the effects of evaporation on capillary flow, we consider the simplest case of uniform evaporation. In this section, we use the rate of evaporation J as the only fitting parameter to fit the no-stress model to capillary-flow experiments of 0.03 w/w aqueous solutions of poly(vinyl alcohol) (PVA) conducted by Lade $et\ al.^{12}$

Solution characterization

While aqueous PVA solution is Newtonian,¹² the viscosity depends on the concentration of PVA as seen in Figure S2a. A four-order-of-magnitude increase in the viscosity is observed for the PVA concentration range of 0-0.12 w/w. In addition to viscosity, surface tension and static contact angle also depend on the concentration of PVA as seen in Figures S2b,c. Based on Figure S2b, a decrease of the surface tension is observed as the PVA concentration increases, while the opposite trend is observed for the static contact angle in Figure S2c.

An empirical viscosity model proposed by Patton⁶³ is used to capture the temperature T and PVA concentration ϕ dependence of the viscosity:

$$\log \bar{\eta} = \frac{\phi}{k_a(T) + \phi k_b(T)}, \quad \text{where} \quad \begin{aligned} k_a(T) &= 1.28 \cdot 10^{-5} T(K) + 1.59 \cdot 10^{-2}, \\ k_b(T) &= 3.83 \cdot 10^{-4} T(K) - 2.47 \cdot 10^{-2}. \end{aligned}$$
(27)

The fitting parameters $k_a(T)$ and $k_b(T)$ reported by Lade¹¹ were obtained by fitting the empirical model to rheological data ranging from 17-40°C, with concentrations ranging from 0.03-0.121 w/w, and over shear rates of 0.1-10 s⁻¹. The empirical model is depicted as a dashed line in Figure S2a.

The empirical formulas used to describe the dependence of the surface tension and static contact angle on the PVA concentration are

$$\bar{\sigma} = 16.378\phi^2 - 3.5713\phi + 1,\tag{28}$$

$$\theta = 2097\phi^2 + 102.84\phi + 19.9,\tag{29}$$

which are obtained by fitting surface-tension and contact-angle measurements conducted by Lade¹¹ at 23°C with PVA concentrations ranging from 0-0.12 w/w. These empirical formulas are represented as dashed lines in Figures S2b,c, respectively.

Equations (27)–(29) are used to describe the concentration-dependent viscosity $\bar{\eta}(\phi)$, surface tension $\bar{\sigma}(\phi)$, and static contact angle $\theta(\phi)$ in eq. (17) to account for effects of evaporation.

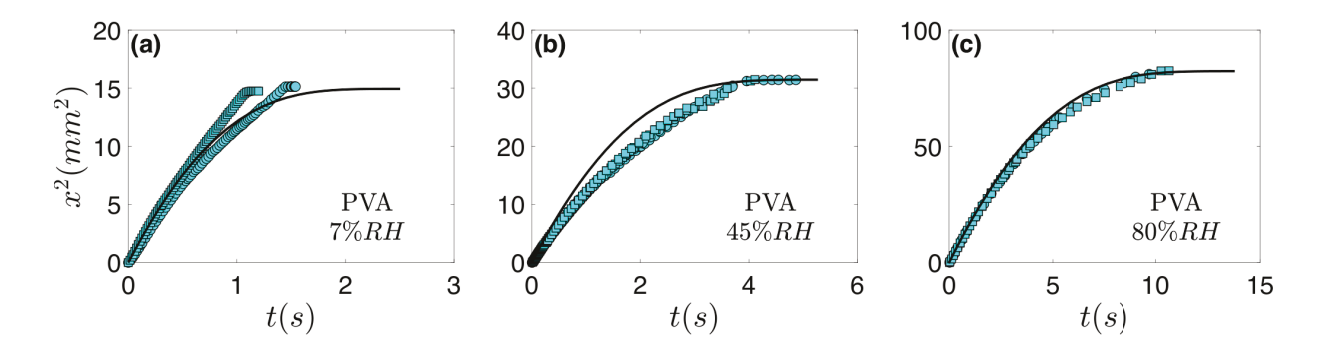


Figure 7: Square of the liquid-front position x^2 as a function of time t for $\lambda = 1.872$ of PVA. The solid symbols representing the experimental results of Lade $et~al.^{12}$ are fitted with the no-stress model for relative humidities (RH) of (a) 7%, (b) 45%, and (c) 80%. The model predictions using the no-stress boundary condition are depicted as solid lines.

Comparison with results of Lade et al.

The effects of evaporation on capillary flow are determined by using the rate of evaporation \bar{J} as the only parameter to fit the no-stress model to experiments conducted by Lade et al.¹² The comparison is depicted in Figure 7 for $\lambda = 1.872$ for different relative humidities RH, which were used to control the rate of evaporation. As the relative humidity increases, the evaporative flux decreases, resulting in longer flow distances and longer flow times.

In the presence of evaporation the mobility parameter k (i.e., slope of solid lines in Figure 7) decreases as a function of time due to the increase in viscosity, decrease in surface tension, and increase in static contact angle, resulting in flow termination. By using the rate of evaporation as the only fitting parameter, the no-stress model is able to capture the liquid-front evolution quantitatively for all three RH conditions depicted in Figure 7.

The validity of the evaporative flux values used to fit the experimental data is assessed by comparison to the bulk drying measurements reported by Lade $et~al.^{12}$ Table 2 illustrates that the flux values used in the model are $\mathcal{O}(10-10^2)$ larger than those observed in the bulk drying experiments. The discrepancy is likely a result of the model assumptions that the liquid height and the evaporation rate, and hence the concentration-dependent viscosity, are spatially uniform.

However, Lade $et\ al.^{12}$ experimentally showed the presence of spatial gradients in the PVA concentration, with solute accumulation at the contact line. This resulted in a non-uniform dry-film thickness after complete solvent evaporation. These findings led Lade $et\ al.^{12}$ to infer that the evaporation rate is enhanced at the contact line and pinning of the contact

line occurs far before drying of the liquid in rest of the channel. This phenomenon is not accounted for in the model or in the bulk evaporation rate data. Hence, the model requires an extremely high uniform evaporation rate to replicate the experimentally observed flow behavior, which is significantly affected by the higher local PVA concentration at the contact line. Despite there being a discrepancy between the evaporative mass fluxes used to fit the model and those obtained from bulk drying experiments, important scaling relationships can be obtained from the model and are discussed in the following section.

Table 2: Comparison of evaporative flux values to flux values obtained by fitting the nostress model to experimental data by Lade *et al.*¹² Reported evaporative mass flux values are in units of mg m⁻² s⁻¹.

Relative Humidity	Evaporative mass flux		
(%)	bulk drying experiments ¹²	model	
7	650	14420	
45	230	6866	
80	90	2630	

Scaling analysis

In many applications relying on capillary flow subject to evaporation, the goal is not necessarily to control the liquid-front evolution but rather the final liquid-front position x_F and the final flow time t_F . The final liquid-front position x_F corresponds to the position where the liquid-front meniscus propagation is halted and the final flow time t_F corresponds to the time at which the liquid meniscus propagation is terminated.

To control the final flow time and final liquid-front position, it is necessary to determine their dependence on the rate of evaporation and the microchannel dimensions. The 1D model is used to determine scaling relationships for the dependence of the dimensionless final flow time \bar{t}_F and dimensionless final liquid-front position \bar{x}_F on the dimensionless evaporative flux \bar{J} and channel aspect ratio λ . Using the height evolution eq. (18), the dimensionless final flow time scales as

$$\bar{t}_F \sim \frac{\lambda}{\bar{J}},$$
 (30)

where the dimensionless final flow time is proportional to the channel aspect ratio $\lambda = H/W$ and inversely proportional to the dimensionless total evaporative mass flux \bar{J} .

Similarly, using the force balance in eq. (17) the dimensionless final liquid-front position scales as

$$\bar{x}_F^2 \sim \frac{\lambda^3 \zeta_o(\lambda)}{\bar{J}}$$
 (31)

where $\zeta_o(\lambda)$ is an aspect-ratio function (see ref. 21). Based on this scaling relationship the dimensionless final liquid-front position is nonlinearly related to the channel aspect ratio and inversely proportional to the square root of the dimensionless evaporative mass flux.

The accuracy of the scaling arguments can be seen in Figure 8 for different channel widths W. The scaling relationships of eqs. (30) and (31) are in agreement with experimental results by Lade $et\ al.^{12}$ We note that the evaporative mass flux values used to define the coordinates of the experimental data points in Figure 8 are the bulk evaporative mass flux values reported by Lade $et\ al.^{12}$ In experiments, the evaporative mass flux will likely be a function of space, but Figure 8 suggests that the constant bulk values are sufficient for qualitatively understanding the behavior of the final liquid-front position and the final flow time. Quantitatively accurate predictions of these quantities and of the time-evolution of the liquid front will likely require accounting for the spatial dependence of the evaporative mass flux (and possibly the influence of temperature-induced surface-tension changes).

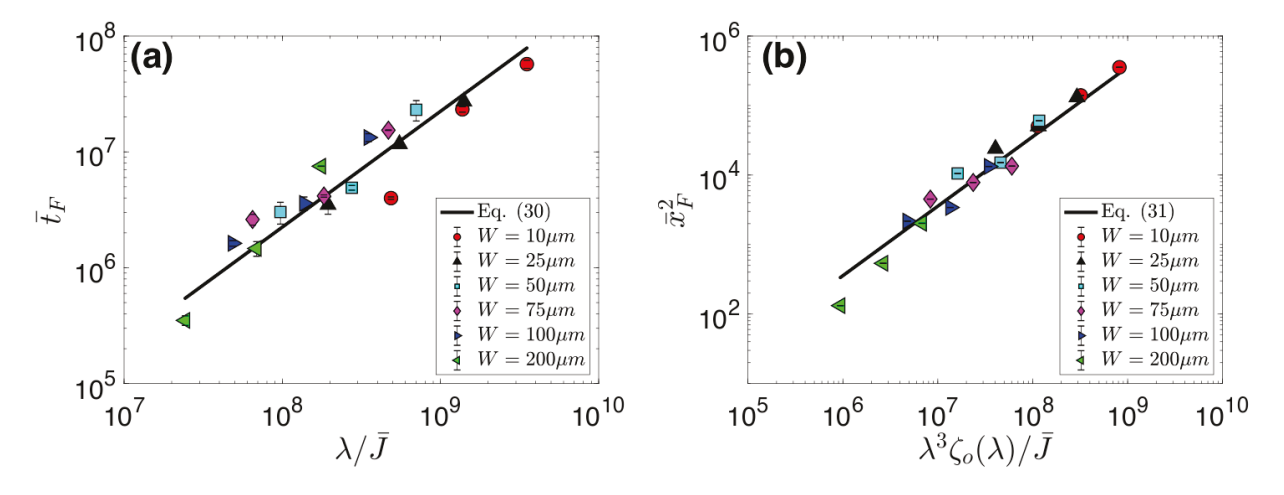


Figure 8: Scaling relationships for (a) dimensionless final time \bar{t}_F and (b) square of the dimensionless final liquid-front position \bar{x}_F^2 , for different channel widths W. The solid lines represent the proposed scalings from eqs. (30) and (31) and the solid symbols represent experimental results by Lade *et al.*¹² All channel heights H are 46.8 μ m.

Conclusions

The results of this study help resolve conflicting results from prior literature regarding the proper boundary condition at the upper liquid-air interface in capillary flows in open rectangular microchannels. Flow visualization experiments indicate the absence of a rigidified liquid-air interface, suggesting that the no-slip boundary condition is not appropriate. The better agreement between model predictions using the no-slip (rather than the no-stress) boundary condition and experimental observations with low-viscosity liquids is likely due to factors not included in the model such as (i) upper and forward meniscus morphology, (ii) dynamic contact angle effects, and (iii) channel roughness. For high-viscosity liquids, the influence of these factors appears to be suppressed by the large bulk viscosity.

We have also developed a Lucas-Washburn-type 1D model that incorporates the effects of concentration-dependent viscosity and uniform evaporation. Scaling relationships obtained from the model for the dependence of the final flow time and final liquid-front position on the rate of evaporation and channel dimensions are in good agreement with experimental observations. The model developed here can be used for any solution or colloidal suspension where the shear viscosity is the dominant rheological parameter, provided that expressions for the concentration-dependent viscosity, surface tension, and contact angle are available. Although the evaporative mass flux was used as a fitting parameter in the present study, more detailed evaporation models could be incorporated. To accurately predict the time-evolution of the liquid front, it will be necessary to use a model that accounts for the upper and forward meniscus morphology, as well as finger formation and dynamics.

Appendix

Ouali et al.²¹ report a general solution to the Navier-Stokes equation relating u(y,z) to the depth- and width-averaged velocity $u_x(t) = dx/dt$ (eq. (3)) for an open rectangular channel, subject to a no-stress boundary condition at the upper liquid-air interface and a no-slip boundary condition on the solid walls. This general solution is given by

$$u(y,z) = -\frac{12u_x}{\pi^3 \lambda^2 \zeta_o(\lambda)} \sum_{n=0}^{\infty} \frac{(-1)^n}{(2n+1)^3} \left[\cosh(a_n^o z/H) - \tanh(a_n^o) \sinh(a_n^o z/H) - 1\right] \cos(a_n^o y/H),$$
(32)

where $\lambda = h/W$ is the aspect ratio based on the liquid height, $-W/2 \le y \le W/2$ and $0 \le z \le h$, $a_n^o = (2n+1)\pi\lambda$, and $\zeta_o(\lambda)$ is an aspect-ratio function defined as

$$\zeta_o(\lambda) = \frac{24}{\pi^4 \lambda^2} \sum_{n=0}^{\infty} \frac{1}{(2n+1)^4} \left[1 - \frac{\tanh(a_n^o)}{a_n^o} \right].$$
 (33)

Using eq. (32) to evaluate the inlet momentum flux term in eq. (2) gives rise to the aspectratio function $f_o(\lambda)$ defined as

$$f_{o}(\lambda) = \frac{1}{hW} \int_{0}^{h(t)} \int_{-W/2}^{W/2} \left[-\frac{12}{\pi^{3} \lambda^{2} \zeta_{o}(\lambda)} \sum_{n=0}^{\infty} \frac{(-1)^{n}}{(2n+1)^{3}} \right] \times \left[\cosh(a_{n}^{o} z/H) - \tanh(a_{n}^{o}) \sinh(a_{n}^{o} z/H) - 1 \right] \cos(a_{n}^{o} y/H) dy dz.$$
(34)

Ouali *et al.*²¹ also report a general solution for an open rectangular channel subject to a no-slip boundary condition at the upper liquid-air interface and on the solid walls, which is equivalent to the general solution for a closed rectangular channel given by

$$u(y,z) = -\frac{48u_x}{\pi^3 \zeta_c(\lambda)} \sum_{n=0}^{\infty} \frac{(-1)^n}{(2n+1)^3} \left[1 - \frac{\cosh(a_n^c y/W)}{\cosh(a_n^c/2)} \right] \cos(a_n^c z/W), \tag{35}$$

where $-W/2 \le y \le W/2$ and $-h/2 \le z \le h/2$, $a_n^c = (2n+1)\pi/\lambda$, and $\zeta_c(\lambda)$ is an aspect-ratio function defined as

$$\zeta_c(\lambda) = \frac{96}{\pi^4} \sum_{n=0}^{\infty} \frac{1}{(2n+1)^4} \left[1 - \frac{2 \tanh(a_n^c/2)}{a_n^c} \right].$$
 (36)

Similar to $f_o(\lambda)$, an aspect-ratio function $f_c(\lambda)$ resulting from evaluation of the inlet momentum flux term for a closed rectangular channel can be obtained using eq. (35).

Acknowledgments

This work was supported by the National Science Foundation (NSF) under Grant No. CMMI-1634263. K.S.J. acknowledges support from the NSF Graduate Research Fellowship Program under Grant No. 00039202. R.K.L. was further supported by the University of Minnesota Graduate School under the Doctoral Dissertation Fellowship (DDF) program. The authors thank Wieslaw Suszynski for assistance with flow visualization and Dan Frisbie for helpful discussions. Portions of this work were conducted in the Minnesota Nano Center, which is supported by the NSF through the National Nano Coordinated Infrastructure Network under Award ECCS-1542202.

Associated Content—Supporting Information

Supporting Information can be found at the end of the manuscript.

Fig. S1. Image sequence of capillary flow. Fig. S2. Plots of viscosity, surface tension, and static contact angle as a function of PVA concentration.

References

- [1] G. M. Whitesides. The origins and the future of microfluidics. *Nature*, 442:368–373, 2006.
- [2] J. P. Brody, P. Yager, R. E. Goldstein, and R. H. Austin. Biotechnology at low Reynolds numbers. *Biophys. J.*, 71(6):3430–3441, 1996.
- [3] A. Marmur and R. D. Cohen. Characterization of Porous Media by the Kinetics of Liquid Penetration: The Vertical Capillaries Model. *J. Colloid Interface Sci.*, 189(2):299–304, 1997.
- [4] N. J. Shirtcliffe, G. McHale, M. I. Newton, F. B. Pyatt, and S. H. Doerr. Critical conditions for the wetting of soils, *Appl. Phys. Lett.*, 89:094101, 2006.
- [5] A. Faghri. Heat pipe science and technology. Global Digital Press, 1995.
- [6] A. Mahajan, W.-J. Hyun, S. B. Walker, G. A. Rojas, J.-H. Choi, J. A. Lewis, L. F. Francis, and C. D. Frisbie. A Self-Aligned Strategy for Printed Electronics: Exploiting Capillary Flow on Microstructured Plastic Surfaces. Adv. Electron. Mater., 1(9):1500137, 2015.
- [7] K. S. Jochem, W. J. Suszynski, C. D. Frisbie, and L. F. Francis. High-Resolution, High-Aspect-Ratio Printed and Plated Metal Conductors Utilizing Roll-to-Roll Microscale UV Imprinting with Prototype Imprinting Stamps. Ind. Eng. Chem. Res., 57(48):16335–16346, 2018.
- [8] M. Cao, K. S. Jochem, W.-J. Hyun, L. F. Francis, and C. D. Frisbie. Self-aligned inkjet printing of resistors and low-pass resistorcapacitor filters on roll-to-roll imprinted plastics with resistances ranging from 10 to 10⁶ Ω. Flex. Print. Electron., 3(4):045003, 2018.
- [9] T. W. Sowers, R. Sarkar, S. E. Prameela, E. Izadi, and J. Rajagopalan. Capillary driven flow of polydimethylsiloxane in open rectangular microchannels. *Soft Matter*, 12:5818–5823, 2016.
- [10] D. Yang, M. Krasowska, C. Priest, M. N. Popescu, and J. Ralston. Dynamics of Capillary-Driven Flow in Open Microchannels. J. Phys. Chem. C, 115:18761–18769, 2011.

- [11] R. K. Lade Jr. Flow and Drying Dynamics in Gravity- and Capillary-Driven Coating Processes, Ph.D. Dissertation, University of Minnesota, Minneapolis, MN, 2017.
- [12] R. K. Lade Jr., K. S. Jochem, C. W. Macosko, and L. F. Francis. Capillary Coatings: Flow and Drying Dynamics in Open Microchannels. *Langmuir*, 34(26):7624–7639, 2018
- [13] T. Chen. Capillary force-driven fluid flow of a wetting liquid in open grooves with different sizes. Proceedings of the 14th IEEE Intersociety Thermal and Thermomechanical Conference, Lake Buena Vista, FL, May 2014; pp 388–396.
- [14] J. Berthier, K. A. Brakke, E. P. Furlani, I. H. Karampelas, V. Poher, D. Gosselin, M. Cubizolles, and P. Pouteau. Whole blood spontaneous capillary flow in narrow V-groove microchannels. Sensor. Actuat. B-Chem., 206:258–267, 2015.
- [15] E. Kim, Y. Xia, and G. M. Whitesides. Polymer microstructures formed by moulding in capillaries *Nature*, 376:581–584, 1995.
- [16] S. Lone, J. M. Zhang, I. U. Vakarelski, E. Q. Li, and S. T. Thoroddsen. Evaporative Lithography in Open Microfluidic Channel Networks. *Langmuir*, 33(11):2861–2871, 2017.
- [17] E. K. Rideal. On the Flow of Liquids under Capillary Pressure. *Philos. Mag.*, 44(264):1152-1159, 1922.
- [18] L. R. Fisher and P. D. Lark. An Experimental Study of the Washburn Equation for Liquid Flow in Very Fine Capillaries. J. Colloid Interface Sci., 69(3):486–492, 1979.
- [19] D. Quéré. Inertial Capillarity. Europhys. Lett., 39(5):533–538, 1997.
- [20] Y. Zhu and K. Petkovic-Duran. Capillary Flow in Microchannels. *Microfluid.* Nanofluid., 8(2):275–282, 2010.
- [21] F. F. Ouali, G. McHale, H. Javed, C. Trabi, N. J. Shirtcliffe, and M. I. Newton. Wetting considerations in capillary rise and imbibition in closed square tubes and open rectangular cross-section channels. *Microfluid. Nanofluid.*, 15(3):309–326, 2013.
- [22] R. Lucas. Ueber das Zeitgesetz des kapillaren Aufstiegs von Flüssigkeiten. Kolloid Z., 23:15–22, 1918.

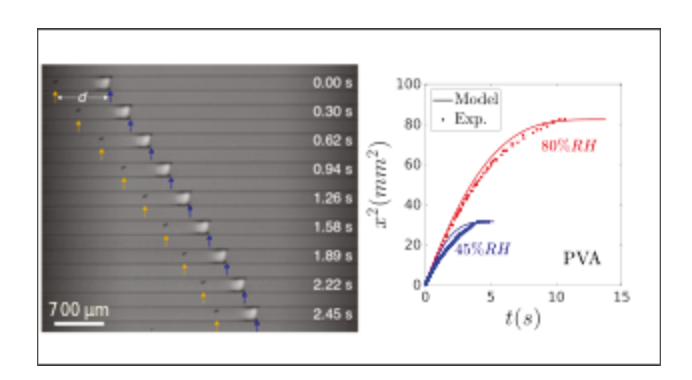
- [23] E. W. Washburn. The Dynamics of Capillary Flow. Phys. Rev., 17(3):273–283, 1921.
- [24] C. H. Bosanquet. On the flow of liquids into capillary tubes. *Philos. Mag.*, 45(267):525–531, 1923.
- [25] J. Szekely, A. W. Neumann, and Y. K. Chuang. The rate of capillary penetration and the applicability of the Washburn equation. J. Colloid Interface Sci., 35(2):273–278, 1971.
- [26] S. Levine, J. Lowndes, E. J. Watson, and G. Neale. A theory of capillary rise of a liquid in a vertical cylindrical tube and in a parallel-plate channel: Washburn equation modified to account for the meniscus with slippage at the contact line. *J. Colloid Interface Sci.*, 73(1):136–151, 1980.
- [27] N. Ichikawa, K. Hosokawa, and R. Maeda. Interface motion of capillary-driven flow in rectangular microchannel. *J. Colloid Interface Sci.*, 280(1):155–164, 2004.
- [28] N. Fries and M. Dreyer. The transition from inertial to viscous flow in capillary rise. *J. Colloid Interface Sci.*, 327(1):125–128, 2008.
- [29] V. Jokinen and S. Franssila. Capillarity in microfluidic channels with hydrophilic and hydrophobic walls. *Microfluid. Nanofluid.*, 5(4):443–448, 2008.
- [30] V. T. Gurumurthy, D. Rettenmaier, I. V. Roisman, C. Tropea, and S. Garoff. Computations of spontaneous rise of a rivulet in a corner of a vertical square capillary *Colloids Surface A*, 544:118–126, 2018.
- [31] J. A. Mann Jr., L. A. Romero, R. R. Rye, and F. G. Yost. Flow of simple liquids down narrow V grooves. *Phys. Rev. E*, 52(4):3967–3972, 1995.
- [32] R. R. Rye, J. A. Mann Jr., and F. G. Yost. The Flow of Liquids in Surface Grooves. Langmuir, 12(2):555–565, 1996.
- [33] F. G. Yost, R. R. Rye, and J. A. Mann Jr. Solder wetting kinetics in narrow V-grooves. Acta Mater., 45(12):5337–5345, 1997.
- [34] R. R. Rye, F. G. Yost, and E. J. O'Toole. Capillary Flow in Irregular Surface Grooves. Langmuir, 14(14):3937–3943, 1998.

- [35] P. S. Ayyaswamy, I. Catton, and D. K. Edwards. Capillary Flow in Triangular Grooves. J. Appl. Mech., 41(2):332–336, 1974.
- [36] L. A. Romero and F. G. Yost. Flow in an open channel capillary. *J. Fluid Mech.*, 322:109–129, 1996.
- [37] M. M. Weislogel and S. Lichter. Capillary flow in an interior corner. *J. Fluid Mech.*, 373:349–378, 1998.
- [38] S. W. Tchikanda, R. H. Nilson, and S. K. Griffiths. Modeling of pressure and shear-driven flows in open rectangular microchannels. *Int. J. Heat Mass Tran.*, 47(3):527–538, 2004.
- [39] V. T. Gurumurthy, I. V. Roisman, C. Tropea, and S. Garoff. Spontaneous rise in open rectangular channels under gravity. *J. Colloid Interface Sci.*, 527:151–158, 2018.
- [40] S. Kachel, Y. Zhou, P. Scharfer, C. Vranic, W. Petrich, and W. Schabel. Evaporation from open microchannel grooves. *Lab Chip*, 14:771–778, 2014.
- [41] S. Levine, P. Reed, E. J. Watson, and G. Neale. A theory of the rate of rise of a liquid in a capillary *In Colloid and Interface Science*, 3:403–419, 1976.
- [42] M. Dreyer, A. Delgado, and H. J. Path. Fluid motion in capillary vanes under reduced gravity. *Microgravity Sci. Technol.*, 5:203–210, 1993.
- [43] M. Dreyer, A. Delgado, and H. J. Path. Capillary rise of liquid between parallel plates under microgravity. *J. Colloid Interface Sci.*, 163(1):158–168, 1994.
- [44] R. J. Good. The rate of penetration of a fluid into a porous body initially devoid of adsorbed material (1, 2). *J. Colloid Interface Sci.*, 42(3):473–477, 1973.
- [45] J.-C. Baret, M. M. Decré, S. Herminghaus, and R. Seemann. Transport dynamics in open microfluidic grooves. *Langmuir*, 23(9):5200–5204, 2007.
- [46] R. L. Panton. Incompressible flow. John Wiley & Sons, 2006.
- [47] V. Lazouskaya, Y. Jin, and D. Or. Interfacial interactions and colloid retention under steady flows in a capillary channel. *J. Colloid Interface Sci.*, 303(1):171–184, 2006.

- [48] V. V. Yaminsky, S. Ohnishi, E. A. Vogler, and R. G. Horn. Stability of aqueous films between bubbles. Part 1. The effect of speed on bubble coalescence in purified water and simple electrolyte solutions. *Langmuir*, 26(11):8061–8074, 2010.
- [49] J. Salter, B. G. Murray, and J. E. Braggins. Wettable and unsinkable: The hydrodynamics of saccate pollen grains in relation to the pollination mechanism in the two New Zealand species of Prumnopitys Phil. (Podocarpaceae). Ann. Bot-London, 89(2):133–144, 2002.
- [50] R. K. Lade Jr., J. O. Song, A. D. Musliner, B. A. Williams, S. Kumar, C. W. Macosko, and L. F. Francis. Sag in drying coatings: Prediction and real time measurement with particle tracking. *Prog. Org. Coat.*, 86:49–58, 2015.
- [51] R. Seemann, M. Brinkmann, E. J. Kramer, F. F. Lange, and R. Lipowsky. Wetting morphologies at microstructured surfaces. P. Natl. Acad. Sci. U.S.A., 102(6):1848– 1852, 2005.
- [52] P. Concus and R. Finn. On the behaviour of a capillary surface in a wedge. *P. Natl. Acad. Sci. U.S.A.*, 63(2):292–299, 1969.
- [53] A. Siebold, M. Nardin, J. Schultz, A. Walliser, and M. Oppliger. Effect of dynamic contact angle on capillary rise phenomena. *Colloid Surface A*, 161(1):81–87, 2000.
- [54] M. N. Popescu, J. Ralston, and R. Sedev. Capillary Rise with Velocity-Dependent Dynamic Contact Angle. *Langmuir*, 24(21):12710–12716, 2008.
- [55] R. G. Cox. The dynamics of the spreading of liquids on a solid-surface. Part 1. Viscous-flow. *J. Fluid Mech.*, 168:169–194, 1986.
- [56] L. M. Hocking. A Moving Fluid Interface on a Rough Surface. J. Fluid Mech., 76(4):801–817, 1976.
- [57] T. D. Blake. The physics of moving wetting lines. J. Colloid Interface Sci., 299(1):1–13, 2006.
- [58] Y. Sui, H. Ding, and P. D. Spelt. Numerical Simulations of Flows with Moving Contact Lines. *Annu. Rev. Fluid Mech.*, 46:97–119, 2014.

- [59] C. G. Ngan and E. B. Dussan V. On the nature of the dynamic contact angle: an experimental study. *J. Fluid Mech.*, 118:27–40, 1982.
- [60] B. Legait and P. Sourieau. Effect of geometry on advancing contact angles in fine capillaries. *J. Colloid Interface Sci.*, 107(1):14–20, 1985.
- [61] E. Vandre, M. S. Carvalho, and S. Kumar. Delaying the onset of dynamic wetting failure through meniscus confinement. *J. Fluid Mech.*, 707:496–520, 2012.
- [62] S. Girardo, S. Palpacelli, A. De Maio, R. Cingolani, S. Succi, and D. Pisignano. Interplay between Shape and Roughness in Early-Stage Microcapillary Imbibition. *Langmuir*, 28(5):2596–2603, 2012.
- [63] T. C. Patton. Paint flow and pigment dispersion. Halsted Press, 1964.

For Table of Contents Only



Supporting Information

Capillary Flow with Evaporation in Open Rectangular Microchannels Panayiotis Kolliopoulos, Krystopher S. Jochem, Robert K. Lade Jr., Lorraine F. Francis, Satish Kumar

Department of Chemical Engineering and Materials Science, University of Minnesota, Minneapolis, MN 55455, USA

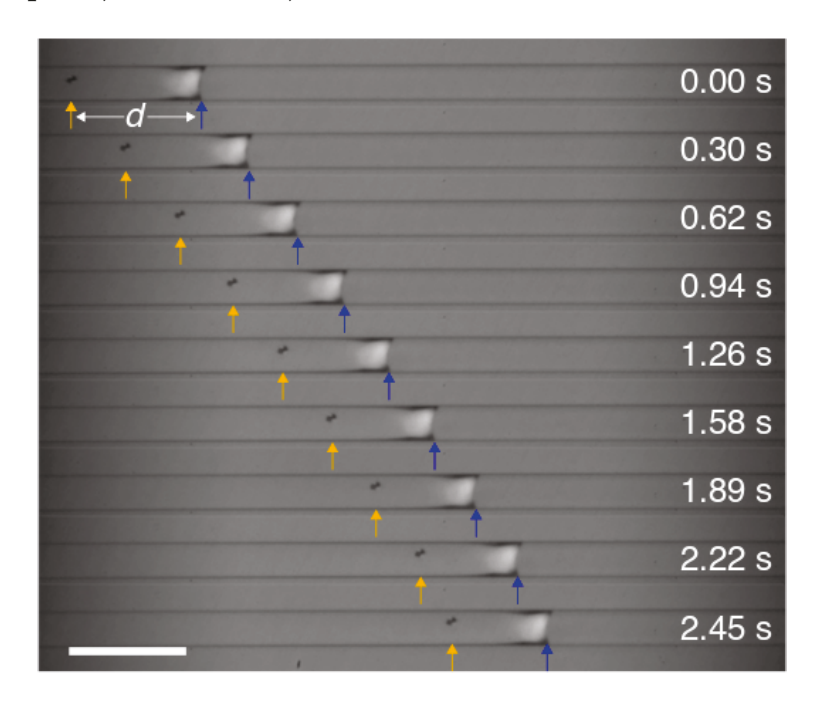


Figure S1: Image sequence of capillary flow of 0.70 w/w aqueous glycerol in 200 μ m wide and 177 μ m deep open rectangular channels. Orange arrows indicate the position of the Lycopodium particles and the blue arrows indicate the position of the advancing liquid front. The Lycopodium particles were initially located a distance d from the liquid front. Scale bar: 700 μ m.

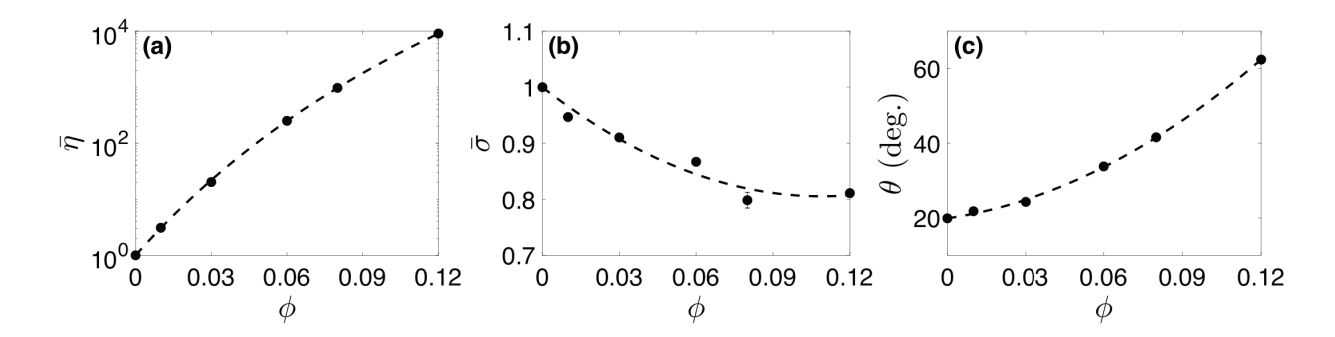


Figure S2: (a) Dimensionless viscosity $\bar{\eta}$, (b) dimensionless surface tension $\bar{\sigma}$, and (c) static contact angle θ as a function of PVA concentration ϕ . Solid symbols represent experimental measurements at 23°C by Lade.¹¹ In panel (a) the dashed line represents an empirical viscosity model proposed by Patton⁶³ accounting for the temperature and the solute-concentration dependence of the viscosity seen in eq. (27). In panel (b-c) dashed lines represent empirical formulas of eqs. (28) and (29), respectively, which were obtained by fitting the experimental data. The solvent viscosity η_0 and surface tension σ_0 used for non-dimensionalization are those of water, shown in Table 1. The reported density is 1.0 g/cm³.¹²